

On Remote Temperature Sensing Using Commercial UHF RFID Tags

Xiangyu Wang, Jian Zhang, Zhitao Yu, Shiwen Mao, *Fellow, IEEE*, Senthilkumar CG Periaswamy, Justin Patton

Abstract—With the fast-growing adoption of the radio-frequency identification (RFID) technology, RFID-based sensors have attracted great interest. Due to the limitation of RFID tags, most existing RFID based temperature sensing works rely on hardware modification, which increases the cost and hampers its deployment. In this paper, we propose RFThermometer, a remote temperature sensing system with commercial Ultra High Frequency (UHF) RFID tags. We first investigate the effect of temperature on RFID phases. To alleviate the precision deterioration caused by missing phase measurements, a tensor completion method is proposed to restore missing phases and a Gaussian Processor model is leveraged to construct a phase-temperature map in the offline stage. In the online stage, the unknown temperature is estimated by a dynamic time warping (DTW) based greedy method. Extensive experimental results are presented to validate the performance of RFThermometer with off-the-shelf RFID devices.

Index Terms—Gaussian Process; RFID; RF sensing; Remote temperature measurement; Tensor completion.

I. INTRODUCTION

With the rapid development of passive radio-frequency identification (RFID) technology, RFID tags have been widely deployed in many areas, such as supply chain management, access control, and inventory tracking [1]. Due to the ubiquitous employment, ease of deployment, and low cost of RFID tags, it is possible and feasible to extend the applications of RFID to healthcare monitoring and environmental sensing. Recently, because of the drastic growth of the Internet of Things (IoT), RFID-based sensing systems have attracted great interest in both industry and academia. RFID-based sensing systems have been developed for gesture recognition [2], localization [3], navigation [4], [5], material detection [6], and breath monitoring [7]. RFID-based sensing systems are able to offer many convenient non-intrusive services, which is also helpful for remote environmental temperature sensing.

Current RFID based temperature sensing systems usually depend on modified RFID tags. Some general sensors can be embedded in RFID tags [8], to provide temperature readings from -40°C to 85°C . However, the sensors could only be used at 134.2 kHz. Experiments show that the operation range of

such tags is limited by the size of the reader antenna. For example, the read range is only 25cm with a square antenna (80×100 mm). To overcome the limitation, Vaz et al. in [9] proposed a specific temperature sensor, which is compatible with Ultra High Frequency (UHF) RFID tags. This design achieves a resolution of 0.035°C within a temperature range from 35°C to 45°C . Even though the sensors offer temperature reading reliably and accurately, the implementation of the temperature sensors increases the tag cost and customer expenses significantly. To avoid such costs, some RFID tags exploit the characteristics of some substrate material to achieve temperature sensing. Babar et al. in [10] utilized paraffin wax as a substrate material for RFID tags for heat sensing. Considering the physical properties and characteristics of the paraffin layer, the changes of layer resulted by heating are irreversible even though the temperature of the tag can be brought back to original state. Thus, such modified tag is not a perfect choice for temperature sensing.

Zannas et al. in [11] also demonstrated the effect of temperature on the material characteristics of the RFID tag. They show that the impact of temperature can change the relative permittivity of the antennas and the tag circuit, as well as the size of the antennas. Thus, the complex impedance of the tag is a function of temperature. Furthermore, Zannas et al. also proposed a temperature sensing method with self-tuning RFID tags in [11] and [12]. To maximize the power extraction efficiency, self-tuning RFID tags utilize a self-tuning circuit to change the impedance of the tags, and to compensate the effect of impedance change caused by temperature change. The authors then propose to leverage the value of the self-tuning capacitance to deduce the temperature. However, the precision of the self-tuning RFID tags based temperature sensing is limited by capacitance values of the self-tuning circuit. To achieve a high-resolution temperature estimation, the specific tags are essential. Thus, there is a strong demand for a temperature estimation system using generic, low-cost UHF RFID tags.

Nowadays, many RFID-based applications leverage the phase of RFID responses to achieve passive sensing [4], [7]. Compared to Received Signal Strength (RSS), phase is much more sensitive to changes in the environment and distance [13]. Many applications benefit from such characteristics of phase. Tagscan [6] makes images of the cross section of a target and detects the material of the target using changes in phase and RSS. RED [14] detects the eccentricity of high-speed rotating machinery by monitoring the change of phase and RSS. RF-IDraw [15] realizes precise trajectory tracing with a multi-resolution positioning algorithm that analyzes

Manuscript received Mar. 16, 2019, revised May 29, 2019, accepted Sept. 6, 2019. This work is supported in part by the US National Science Foundation (NSF) under Grants CNS-1702957 and ECCS-1923163. This work was presented in part at IEEE ICC 2019, Shanghai, China, May 2019.

X. Wang, Z. Yu, and S. Mao are with the Department of Electrical and Computer Engineering, Auburn University, Auburn, AL 36849-5201, USA. J. Zhang, S.C.G. Periaswamy, and J. Patton are with Auburn University RFID Lab, Auburn, AL 36849. Email: xzw0042@auburn.edu, jzz0043@auburn.edu, zzy0021@auburn.edu, smao@ieee.org, senthil@auburn.edu, jbp0033@auburn.edu.

RFID phases. RIO [2] is a pervasive touch gesture interface, which tracks fingers by monitoring the phase changes caused by human touch on RFID tags. Even though such localization and recognition applications are successful, there has been no work on temperature monitoring using unmodified, generic RFID tags.

In this paper, we propose to use unmodified, commercial RFID tags for remote temperature sensing [16]. The system not only is cost-effective, since it is implemented with commercial tags, antennas, and reader, but also incorporates advanced signal processing/machine learning techniques, such as tensor completion and Gaussian Process, to ensure high accuracy and robustness. Our target environment includes the refrigerated warehouses and refrigerated retail display cases, etc., where the RFID tagged items are stationary against the RFID readers and antennas in most of the times. In such circumstance, the position of antennas and tags are fixed. Thus, the relative position between tags and readers does not affect the phase reading of backscattered signals. The proposed system will greatly benefit the industry. The cost of the cold chain will be significantly reduced by automatically monitoring temperature with existing commodity RFID tags. Moreover, the ability of remotely monitoring temperature from RFID tags provides detailed information for temperature management.

A particular challenge of using generic tags is the long delay caused by missing phase readings. In a UHF RFID system, if tags are interrogated simultaneously, the modulated signals will collide, and no information is backscattered to the reader. To avoid the collision problem, slotted ALOHA based anti-collision protocols are used in current standard EPCglobal Class 1 Generation 2 [17]. The UHF RFID readers operate on a large number of channels to avoid interference. For example, an RFID system in the USA operates in the 902 ~ 928 MHz band, which is divided into 50 non-overlapping channels, and hops among these channels during interrogation, as required by the Federal Communications Commission (FCC). However, the channel hopping mechanism hampers the continuous observation of a specific channel even though it enhances the data transmission rate of RFID systems. Phase reading of a channel loses frequently in a complex environment, where there are multiple RFID tags and more than one reader. It is difficult to obtain phases from all the 50 channels from one tag in one reading cycle, when many tags are interrogated simultaneously. For example, a zebra RFID reader, FX9600, is leveraged in our RFThermometer system. The reader interrogates tags with 50 channels in sequence. Interrogation takes about 0.1 seconds in each channel. In other words, if a phase information is missing in one channel, it has to wait 5 seconds at least to acquire the phase information from the same channel. Such channel hopping mechanism prolongs the time for collecting enough phases for estimating the temperature. Also, the temperature of a tag could change during the long period of data collection. Actually, any RFID reader that is compatible with EPCglobal Class 1 Generation 2 is friendly to our proposed RFThermometer system.

To this end, we propose to utilize a big data analytics technique, i.e., *tensor completion*, to restore the lost phase

samples. We then use the recovered phase data to model the phase-temperature relationship with a machine learning technique, i.e., *Gaussian Process*, based approach. Specifically, to reduce the data collection time, we employ tensor completion to restore the missing phases, which has been successfully applied to color image recovery [18], video recovery [19], and noise reduction [20]. We create a sparse phase tensor with the phases collected in one round of reading, upon which tensor completion is then applied to restore the missing phase readings. The restored phase tensor is unfolded to obtain a phase matrix, which is then leveraged to model the phase-temperature relationship with Gaussian Process, in the form of a phase-temperature map.

In particular, we present RFThermometer, a temperature measurement system with unmodified, generic RFID tags. In RFThermometer, phases are collected first from different temperatures with the Zebra FX9600 reader [21]. A phase tensor is generated by the collected data and the missing data are then restored by tensor completion. The restored tensor is then unfolded to generate a phase matrix, which includes the phases of sampled temperatures on 50 channels. With Gaussian Process, the relationship between temperature and phase on the 50 channels is learned from the phase matrix. The phase-temperature map of 50 channels is constructed with Gaussian Process and regression. In the online stage, the tensor completion is also applied to restore the missing phases in newly sensed data. We then propose a dynamic time warping (DTW) method to compare the similarity between the newly collected test phases and the phases in the phase-temperature map. A greedy method is used to determine the estimated temperature.

The main contributions of this paper are summarized below.

- To the best of our knowledge, this is the first work to employ tensor completion for restoring missing phases, which effectively reduces the time consumption of phase data collection, and it helps to avoid the degradation of map resolution caused by inadequate data collection.
- We design a Gaussian Process model to regress the relationship between phase and temperature, as well as a DTW based greedy method to improve the accuracy of estimated tag temperature.
- We implement the proposed RFThermometer system with commercial RFID tags, antennas, and reader. Our extensive experimental results demonstrate that RFThermometer is capable to provide temperature estimation with an mean error of 5°C when the phase tensor only includes 10 phases from each channel and the phases are collected from only 10 temperatures. The results demonstrate the robustness and feasibility of the RFThermometer system, as well as the flexible trade-off between time/computation and temperature resolution that RFThermometer offers.

In the remainder of the paper, the preliminaries are introduced in Section II. We present the RFThermometer system in Section III and our performance evaluation in Section IV. Section V summaries this paper.

Notation Boldface Euler script symbols represent tensors, e.g., \mathcal{M} ; bold upper case symbols denote matrices, e.g., \mathbf{M} ;

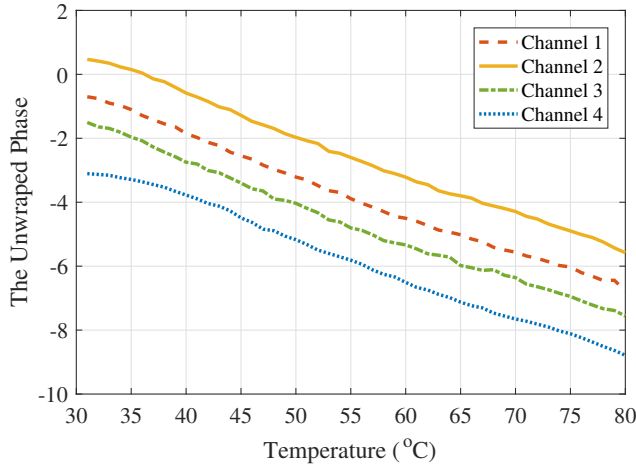


Fig. 1. The phase-temperature relationship measured on four different channels from an RFID tag.

bold lower case symbols stand for vectors, e.g., \mathbf{m} , and the entries are denoted by lower case symbols, e.g., m_{ij} ; the superscript \mathbf{m}^T represent the transpose operator.

II. PRELIMINARIES

A. Passive RFID and Phase-Temperature Relationship

Passive RFID tags rely on a method called backscattering to communicate with readers. The chip on the passive RFID tag harvests energy from the received interrogating signal sent by the reader, and responds by varying its input impedance and thus modulating the backscattered signal with ON-OFF keying. According to [22], the maximum power transfer occurs when the power transmission coefficient reaches the maximum. The power transmission coefficient, α , is given by

$$\alpha = \frac{4R_c R_a}{|Z_c + Z_a|^2}, \quad (1)$$

where R_c , Z_c , R_a and Z_a are the chip resistance, the chip impedance, the antenna resistance, and the antenna impedance, respectively. When the chip impedance and the antenna impedance are conjugately matched, the power transmission coefficient will reach the maximum.

According to [11], the impedance of the tag is affected by the tag temperature. Consequently, the phase of a backscattered signal is affected by the temperature of the tag as well. To understand the relationship between the phase of backscattered signals and the temperature of the tag, we interrogate a single RFID tag over a temperature interval of 50°C. Fig. 1 plots the phases from an RFID tag at increased tag temperature. It can be seen that the phase changes evenly with increased temperature of the tag on each of the four channels. Because of the roughly linear relationship, it is possible for us to model the phase-temperature relationship with a few phase samples at different temperatures.

B. Tensor Completion Preliminaries

Low-rank tensor estimation (LRTE) becomes a hot topic attracting researcher's attention. It has been used in many

areas, such as signal processing and RF sensing [23]. LRTE relies on low-rank tensor decomposition. CP decomposition and Tucker decomposition [24] are the two major tensor decomposition techniques. However, CP decomposition is susceptible to the ill-posedness issue [25], while Tucker decomposition suffers from being trapped at a local minimum, which is a common issue for non-convex optimization [24]. To this end, Tensor-Singular Value Decomposition (t-SVD) is proposed to overcome such drawbacks. Based on t-SVD, the associated notion of tensor multi-rank and its convex relaxation to the corresponding Tensor Nuclear Norm (TNN) for completion and recovery of multilinear data are introduced in [26]. In the RFThermometer system, we employ a t-SVD based multilinear data completion method for restoring missing phase values.

Some essential definitions and equations of tensor decomposition are given below. The nuclear norm of an $n \times n$ matrix \mathbf{M} , $\|\mathbf{M}\|_*$, is defined as [27]

$$\|\mathbf{M}\|_* = \sum_{k=1}^n \beta_k(\mathbf{M}), \quad (2)$$

where $\beta_k(\mathbf{M})$ stands for the k th largest singular value of \mathbf{M} .

For an N -mode tensor $\mathcal{M} \in \mathbb{C}^{a_1 \times \dots \times a_N}$, the mode- i unfolding $\mathbf{M}^{(i)} \in \mathbb{C}^{a_i \times (a_1 \dots a_{i-1} a_{i+1} \dots a_N)}$. Furthermore, the i -th frontal slice of tensor $\mathcal{M} \in \mathbb{C}^{a_1 \times a_2 \times a_3}$ is denoted as $\mathbf{M}_{(i)}$, which is a matrix with size $a_1 \times a_2$. Based on these tensor operations, block-based operators are introduced [28]. For $\mathcal{M} \in \mathbb{C}^{a_1 \times a_2 \times a_3}$, a block circulant matrix is given by

$$\text{bcirc}(\mathcal{M}) = \begin{bmatrix} \mathbf{M}_{(1)} & \mathbf{M}_{(a_3)} & \mathbf{M}_{(a_3-1)} & \dots & \mathbf{M}_{(2)} \\ \mathbf{M}_{(2)} & \mathbf{M}_{(1)} & \mathbf{M}_{(a_3)} & \dots & \mathbf{M}_{(3)} \\ \vdots & \ddots & \ddots & \ddots & \vdots \\ \mathbf{M}_{(a_3-1)} & \mathbf{M}_{(a_3-2)} & \dots & \mathbf{M}_{(1)} & \mathbf{M}_{(a_3)} \\ \mathbf{M}_{(a_3)} & \mathbf{M}_{(a_3-1)} & \dots & \mathbf{M}_{(2)} & \mathbf{M}_{(1)} \end{bmatrix}.$$

The bvec operation and vfold operation are opposite operations, which are defined as

$$\text{bvec}(\mathcal{M}) = [\mathbf{M}_{(1)} \mathbf{M}_{(2)} \dots \mathbf{M}_{(a_3)}]^T \quad (3)$$

$$\text{vfold}(\text{bvec}(\mathcal{M})) = \mathcal{M}. \quad (4)$$

The bdiag operation and bfold operation are also opposite operations as well, which are defined as

$$\text{bdiag}(\mathcal{M}) = \begin{bmatrix} \mathbf{M}_{(1)} & & \mathbf{0} \\ & \ddots & \\ \mathbf{0} & & \mathbf{M}_{(a_3)} \end{bmatrix}, \quad (5)$$

$$\text{bfold}(\text{bdiag}(\mathcal{M})) = \mathcal{M}. \quad (6)$$

The t -product of a mode-3 tensor \mathcal{M} of size $j \times k \times l$ and a mode-3 tensor \mathcal{Q} of size $k \times b \times l$ is given by

$$\mathcal{K} = \mathcal{M} * \mathcal{Q} = \text{vfold}(\text{bcirc}(\mathcal{M}) \cdot \text{bvec}(\mathcal{Q})). \quad (7)$$

The result of t -product $\mathcal{M} * \mathcal{Q}$ is a mode-3 tensor with size $j \times b \times l$. In the Fourier domain, the product of frontal slices of the two mode-3 tensors is represented by

$$\mathcal{K}_{(k)}^f = \mathcal{M}_{(k)}^f \cdot \mathcal{Q}_{(k)}^f, \quad (8)$$

where $\mathcal{K}_{(k)}^f$ is the k -th frontal slice of the Fourier transform of \mathcal{K} along the third dimension. \mathcal{K}^f is the representation of \mathcal{K}

in the Fourier domain. Based on the t-product, the t-SVD of tensor \mathcal{M} is defined as

$$\mathcal{M} = \mathcal{U} * \mathcal{S} * \mathcal{V}^T, \quad (9)$$

where the size of tensor \mathcal{M} is $a_1 \times a_2 \times a_3$; \mathcal{U} and \mathcal{V} are orthogonal tensors of size $a_1 \times a_1 \times a_3$ and $a_2 \times a_2 \times a_3$, respectively; and \mathcal{S} is a f-diagonal tensor with size $a_1 \times a_2 \times a_3$. For a f-diagonal tensor, each of its frontal slice is a diagonal matrix. Similar to matrix SVD, \mathcal{M} is a sum of outer products of matrices, given by [29]:

$$\mathcal{M} = \sum_{j=1}^{\min(a_1, a_2)} \mathcal{U}(:, j, :) * \mathcal{S}(j, j, :) * \mathcal{V}(:, j, :)^T, \quad (10)$$

where the indexing method is similar to Matlab's indexing, e.g., $\mathcal{U}(:, j, :)$ is the j th frontal slice of \mathcal{U} . According to (5) and (8), we have

$$\text{bdiag}(\mathcal{M}^f) = \text{bdiag}(\mathcal{U}^f) \cdot \text{bdiag}(\mathcal{S}^f) \cdot \text{bdiag}(\mathcal{V}^f)^T. \quad (11)$$

Similar to the nuclear norm of a matrix, the nuclear norm (TNN) of a tensor \mathcal{M} is defined as

$$\|\mathcal{M}\|_{TNN} = \sum_{j=1}^{\min(a_1, a_2)} \sum_{k=1}^{a_3} \mathcal{S}^f(j, j, k). \quad (12)$$

Owing to the unitary invariance of the matrix nuclear norm and the block diagonalization property of block circulant matrices [29], we have

$$\|\text{bdiag}(\mathcal{M}^f)\|_* = \|\text{bdiag}(\mathcal{S}^f)\|_* = \|\mathcal{M}\|_{TNN} \quad (13)$$

$$= \|(\mathbf{F} \otimes \mathbf{I}_2) \text{bcirc}(\mathcal{M}) (\mathbf{F}^* \otimes \mathbf{I}_1)\|_* \\ = \|\text{bcirc}(\mathcal{M})\|_*, \quad (14)$$

where \mathbf{F} is the normalized discrete Fourier Transform matrix of size $a_3 \times a_3$; \mathbf{I}_1 and \mathbf{I}_2 are identity matrices with size $a_1 \times a_1$ and $a_2 \times a_2$, respectively; and \otimes stands for the Kronecker product. Following (13) and (14), we have

$$\|\text{bcirc}(\mathcal{M})\|_* = \|\mathcal{M}\|_{TNN}, \quad (15)$$

where $\|\text{bcirc}(\mathcal{M})\|_*$ is the nuclear norm of $\text{bcirc}(\mathcal{M})$, which is obtained by unfolding \mathcal{M} circularly. The nuclear norm exploits the information of \mathcal{M} in multidimension.

When \mathcal{M} is a mode-3 tensor, such as a temperature-phase tensor used in RFThermometer, the relationship between channel and phase, the relationship between temperature and phase, and the observation redundancy could be depicted by the nuclear norm of $\text{bcirc}(\mathcal{M})$. Thus, it is possible to restore the missing phase values on a specific channel at a specific temperature with the help of the matrix nuclear norm of $\text{bcirc}(\mathcal{M})$ or the tensor nuclear norm of \mathcal{M} . The detailed completion method will be presented in the next section.

III. THE RFTHERMOMETER SYSTEM

A. System Architecture

RFThermometer is a fingerprinting based remote temperature sensing system, which operates with an offline stage and an online stage. The system architecture is shown in Fig 2. In the offline stage, the phase values are first collected

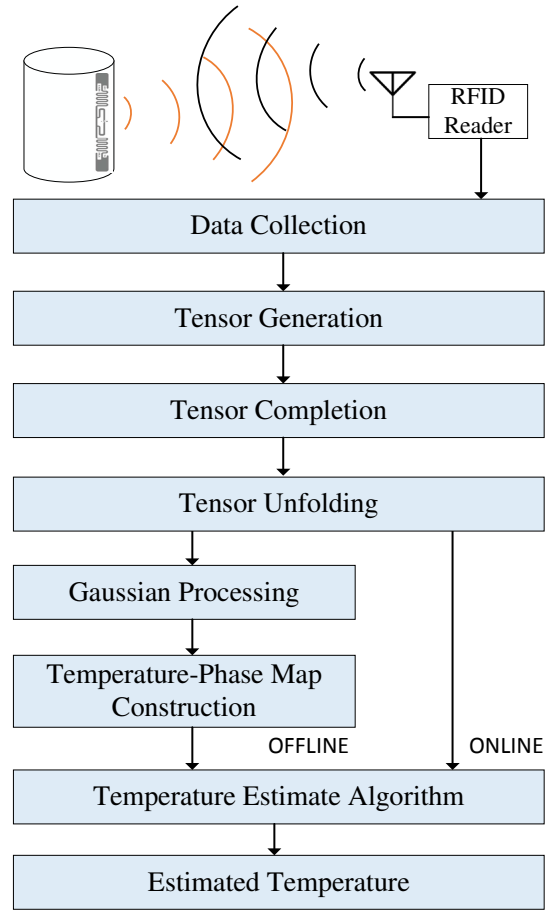


Fig. 2. The RFThermometer system architecture.

from available channels and labeled by the corresponding temperatures. In our proposed system, the FX9600 reader is able to collect phases from 50 channels within a period of 5 seconds. We denote the data collected in one reading cycle as an *observation*, which includes the phases collected from channel 1 to channel 50. Considering the relatively short channel occupancy time, we assume that the phases collected in one cycle share the same temperature label.

In the offline stage, the phases collected within a specific temperature interval could be represented by an order-3 tensor as shown in Fig. 3(a). Because of the dynamic environment and the number of tags, it is usually inevitable to lose phase readings in some channels, which hurt our temperature prediction precision. To overcome the effect caused by the loss of phase readings, we proposed a tensor completion method to recover the lost phases. Compared with traditional regression methods, tensor completion is able to learn the high-order correlation from data and recover the unknown data with the learned correlation. Multi-Linear Gaussian Process (MLGP) is also a popular machine learning algorithm in data recovery, but it depends on the optimized hyper-parameter to achieve the best performance in regression. The 1-D Gaussian Process could not effectively leverage the multidimensional information. To get rid of the burdensome hyper-parameter optimization and increase the phase recovery precision, low rank tensor completion is utilized in RFThermometer because

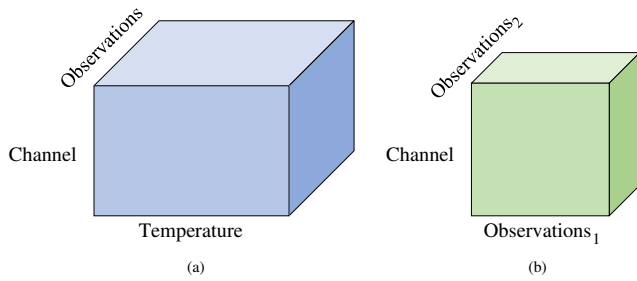


Fig. 3. The phase tensors: (a) a phase tensor in the offline stage, (b) a phase tensor in the online stage

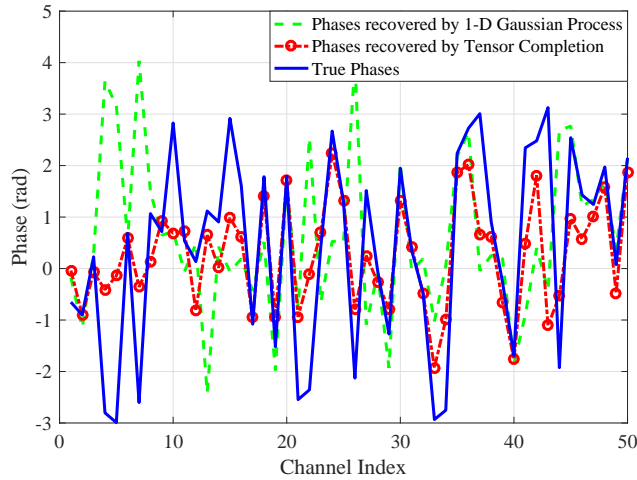


Fig. 4. The phase pattern of 41°C, including the true phase and those recovered by 1-D Gaussian Process and tensor completion.

of its high computational efficiency and easiness to implement.

Although tensor completion and Gaussian Process are employed in the offline stage, their relatively high time complexity does not affect the user experience in the online stage. To demonstrate the necessity of tensor completion, we conducted a benchmark experiment, the results are given in Fig. 4. It plots the phase pattern at 41°C, which includes the phases collected from all the 50 channels. The blue line represents the true phases. The red line and green line represent the phases recovered by tensor completion and 1-D Gaussian Process, respectively. To ensure fairness, the inputs to both algorithms are identical, which includes 10% of the true phases. The mean distance between the true phases and the phases recovered by tensor completion is 0.918 rad, while the mean distance between the true phases and the phases recovered by 1-D Gaussian Process is 1.5934 rad. Apparently, tensor completion could recover the lost phases precisely. Compared to Gaussian Process, the phases recovered by tensor completion are more reasonable. According to Fig. 4, the phases recovered by Gaussian Process on channel 4, channel 7, and channel 26 are larger than π , which are impossible values (since phase readings are rounded to remain in $[-\pi, \pi]$). Thus, the tensor completion is used in our RFThermometer system for better precision of phase recovery.

With the restored phases, a one-dimensional Gaussian Process is next employed for regressing the model of phase-

temperature relationship. Compared with randomness of phase losses on the channels, the phases are sampled in temperature evenly. Fig. 1 shows the rough linearity of the relationship between phase and temperature, which indicates that Gaussian Process should be effective to capture the relationship between phase and temperature. Furthermore, to maintain the flexibility of the system, the phase-temperature model of each channel is constructed by Gaussian Process independently. The well-trained models depict the relationship between the phase and temperature of the corresponding channel. Based on the model we built, the resolution of the temperature-phase map could be decided in the online stage. The variable resolutions of map offer users a trade-off between precision and computational complexity.

In the online stage, new phase observations are collected in a short period. We assume the temperature does not change within the period. Test tensors, as is shown in Fig. 3(b), are constructed with the new phases observations. Note that the number of observations is the sum of *observation₁* and *observation₂*. Similarly, the missing phases in the new observations are recovered by tensor completion. The completed testing tensor is unfolded, and the result is compared with the phases of specific temperatures in the temperature-phase map. By leveraging the temperature-phase map, the temperature associated with the new phase values is estimated by using a dynamic time warping based greedy method.

To the best of our knowledge, RFThermometer is the first system that is focused on remote temperature sensing with unmodified UHF RFID tags. Compared with prior works, RFThermometer does not rely on a temperature sensor embedded in RFID tags, which increases the cost of the system. Moreover, a user can determine the temperature precision to trade-off computation and storage. Based on the temperature-phase model, different temperature-phase maps with variable resolutions can be easily generated. A high-resolution map offers more accurate temperature estimations, but more space is required to store the map and longer time is taken to estimate the unknown temperature in the online estimation. Alternatively, a low-resolution map provides a low precision but it requires smaller storage space and takes shorter computation time.

B. Tensor Completion for Channel Information Recovery

As discussed in Section II-B, the nuclear norm of a block circulant matrix represents the multidimensional information of a tensor, which is equal to the tensor nuclear norm. Thus we consider a tensor nuclear norm penalized algorithm for tensor completion to recover the missing phase readings on some channels. According to [26], [30], the missing phase values can be restored by solving the following convex optimization problem.

$$\min \|\mathcal{X}\|_{TNN} \quad (16)$$

$$\text{s. t. } \mathcal{X}_\Gamma = \mathcal{M}_\Gamma. \quad (17)$$

For the temperature-phase tensor completion problem, \mathcal{X} and \mathcal{M} in (16) are mode-3 tensors with identical size. The entries of \mathcal{X} in the set Γ are known, such as the phase readings

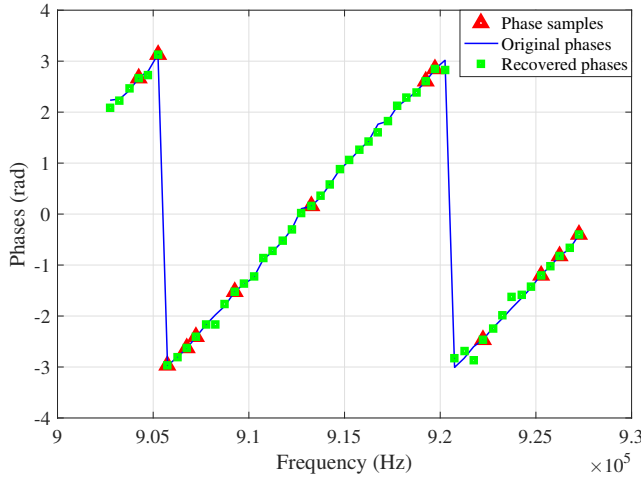


Fig. 5. Phases restored by the tensor completion method.

at some temperatures from some channels. The remaining entries of \mathcal{X} are missing. The missing entries in \mathcal{X} should be restored such that the tensor nuclear norm of \mathcal{X} is as small as possible. Using the general framework of Alternating Direction Method of Multipliers (ADMM) [31], the convex optimization problem (16) can be solved and the solution is given by

$$\mathcal{X} = \mathcal{M}_\Gamma + \left(\mathcal{Y} - \frac{1}{\alpha} \mathcal{M} \right)_{\bar{\Gamma}}, \quad (18)$$

where \mathcal{Y} and \mathcal{M} are tensors that are introduced to solve the convex problem, and $\bar{\Gamma}$ is the complementary sets of Γ .

The tensor completion shows its accuracy in phase restoration. As an example, Fig. 5 shows the phases restored by tensor completion. The original phases are collected from all the 50 channels when the temperature is 46°C. The missing phases are restored with a phase tensor that includes 30% of the phase samples of the original phases (i.e., 70% of the phase readings are missing). In Fig. 5, the green stars, the red triangles, and the blue line represent the restored phases, the known phase samples, and the original phases (i.e., the ground truth), respectively. Apparently, all the green stars (i.e., the restored phases), are on the blue line, which means that the missing phases are successfully restored with only 30% of known phase samples. Furthermore, Fig. 6 presents the cumulative distribution function (CDF) of estimation errors between the true phases and the restored phases. In Fig. 6, when only 30% phase samples are available, 90% of the errors are under 0.02 rad, which is lower than thermal noise. When 10% phase samples are available, our phase restoring algorithm can still guarantee the phase error be smaller than 0.08 rad for 80% of restored phases. We use the restored phases as inputs to the following procedures in RFThermometer, thus saving considerable time and efforts to collect phase samples, which is helpful especially when there are a large number of tags.

C. Gaussian Process for Generating Phase-Temperature Map

To model the relationship between phase and temperature on each of the channels, we propose to employ Gaussian Process

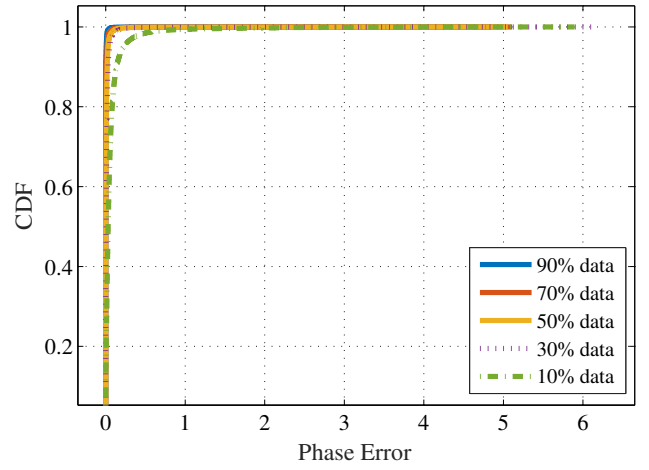


Fig. 6. CDF of phase errors between the truth phases and restored phases that are generated by the tensor completion method.

to build the phase-temperature model (or, map), which can effectively leverage the phases that are restored by tensor completion. Gaussian Process is a collection of random variables, where any finite subset of the random variables has a joint multivariate Gaussian distribution depicted by its mean and covariance function. In RFThermometer, the phase value is given by

$$\theta(t) = p(t) + \delta + \zeta, \quad (19)$$

where $\theta(t)$ is the measured phase at temperature t , $p(t)$ is the true phase at temperature t , δ is the hardware offset, and ζ is the thermal noise. Consider two phase readings $\theta(t_1)$ and $\theta(t_2)$ obtained for temperatures t_1 and t_2 , respectively. They have a joint Gaussian distribution with covariance $k(\theta(t_1), \theta(t_2))$. In our system, we choose the squared exponential function as kernel function, which is defined as

$$k(\theta(t_1), \theta(t_2)) = \lambda^2 \exp \left\{ -\frac{(\theta(t_1) - \theta(t_2))^2}{2d^2} \right\}, \quad (20)$$

where d is a lengthscale and λ is the phase variance, which are updated in the training process of offline stage.

The predictive equations for unknown temperatures are

$$\begin{cases} \Pr(p(t_*)|\tau, \Theta, t_*) = \mathcal{N}(p(t_*); v_*, \lambda_*^2) \\ v_* = \mathbf{k}_*^T (\mathbf{K} + \lambda_n^2 \mathbf{I})^{-1} \Theta \\ \lambda_*^2 = k(\theta(t_*), \theta(t_*)) - \mathbf{k}_*^T (\mathbf{K} + \lambda_n^2 \mathbf{I})^{-1} \mathbf{k}_*, \end{cases} \quad (21)$$

where t_* represents the unknown temperature, τ and Θ are the known temperatures and corresponding phases, respectively, \mathbf{k}_* is used to denote the vector of covariances between the unknown temperatures and known temperatures, \mathbf{K} is the covariance matrix of training temperatures τ , and \mathbf{I} is the identical matrix. To estimate the unknown phases of temperatures, denoted as Θ_{est} , we minimize the loss function $\mathcal{L}(\Theta_{tru}, \Theta_{est})$, where $\Theta_{tru} = p(t_*)$ is the true phase. In RFThermometer, we choose mean square error as loss function, i.e.,

$$\mathcal{L}(p(t_*), \Theta_{est}) = (p(t_*) - \Theta_{est})^2. \quad (22)$$

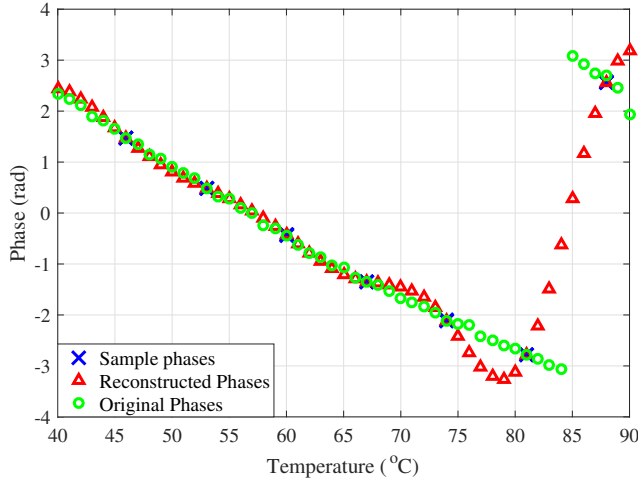


Fig. 7. Phase reconstructed with phase data collected from 10% of the temperatures (marked as blue cross).

As in [32], we have

$$\mathcal{R}_{\mathcal{L}}(\Theta_{est}|t_*) = \int \mathcal{L}(p(t_*), \Theta_{est}) \Pr(p(t_*)|t_*, \mathcal{E}) d\Theta,$$

where $\mathcal{E} = \{(\Theta_i, t_i) | i = 1, 2, \dots, n\}$. Finally, the reconstructed phases are given by

$$\Theta_{rec}|t_* = \underset{\{\Theta_{est}\}}{\operatorname{argmin}} \mathcal{R}_{\mathcal{L}}(\Theta_{est}|t_*). \quad (23)$$

Fig. 7 presents the reconstructed phases on channel 48, which are obtained using the phases collected from 10% of the temperatures. In Fig. 7, the green circles denote the original phase samples (i.e., ground truth), blue crosses stand for the phases samples from the original data that are actually used, and red triangles are the reconstructed phases. It is obvious that both the triangles and circles overlap closely for most of the temperatures. Most errors occur when the temperature is close to 80°C, because the phase rotation happens at this temperature for channel 48 (i.e., a sudden jump from $-\pi$ to π). Fortunately, phase rotation happens at different temperatures for different channels. The effect caused by phase rotation could be effectively eliminated by using phases from multiple channels. For channel 48, the root mean square error (RMSE) between the original phases and reconstructed phases is 0.14 rad within the range that is not affected by the phase rotation. It is safe to say that Gaussian Process is capable of restoring the unknown phases with the phases collected from only 10% of the temperatures. With tensor completion and Gaussian Process, a temperature-phase map \mathcal{H} is constructed in the offline stage. It consists of the temperature-phase relationship over 50 channels for temperatures in $[t_1, t_n]$, as

$$\mathcal{H} = [\mathbf{h}_{t_1}, \mathbf{h}_{t_2}, \dots, \mathbf{h}_{t_n}], \quad (24)$$

where \mathbf{h}_{t_i} is a 50-element column phase vector for temperature t_i , $i = 1, 2, \dots, n$, which consists of the reconstructed phases on all the 50 channels.

D. Temperature Estimation

In the online stage, newly collected phase observations at an unknown temperature are used to build a phase tensor,

as shown in Fig. 3(b). The phases are collected in a short period of time during which the temperature is assumed to be constant. It is common that the amount of phase values is lower than that collected in the offline stage even though the tensor completion is applied. To further mitigate the effect of missing phases, we use Dynamic Time Warping (DTW) [23] in RFThermometer to calculate the similarity between the new testing phases and the phases stored in the temperature-phase map. DTW is different from Euclidean distance, which is the sum of the distances between corresponding point-pairs in two sets. Sets processed by Euclidean distance method have to be in the same size. However, DTW is an optimal matching method, which is capable of handling sets of different sizes. Moreover, it avoids re-sampling, which usually leads to loss of information or introducing fake information.

In RFThermometer, the test tensor \mathcal{R} is processed with tensor completion and the result is unfolded to generate a matrix, \mathbf{S} , which is comprised with observations, given by

$$\mathbf{S} = [\mathbf{s}_1, \mathbf{s}_2, \dots, \mathbf{s}_{a \times b}], \quad (25)$$

where \mathbf{s}_i is an observation that contains phase readings from all 50 channels. In RFThermometer, the size of the test tensor \mathcal{R} is set to $50 \times 2 \times 2$. As shown in Fig. 3(b), the tensor is a sparse tensor which includes 4 observations (i.e., $observation_1 = 2$ and $observation_2 = 2$).

The pseudocode for the online temperature estimation algorithm is presented in Algorithm 1. The inputs to the algorithm are the phase-temperature map \mathcal{H} , which is obtained with Gaussian Process in the offline stage, and the test tensor \mathcal{R} . In the algorithm, the unknown phases in the test tensor is first recovered. The completed tensor, \mathcal{S} , is unfolded along mode-1 to generate the test matrix, \mathbf{S} , which consists of $a \times b$ observations. Next, phases from all 50 channels for each temperature are used to compare with each observation in the test matrix. To better evaluate the similarity between the phase vector \mathbf{h}_{t_j} from the map and the observation vector \mathbf{s}_i from the test matrix, a DTW method is incorporated to calculate the distance between these two vectors, given by

$$\begin{aligned} \mathbf{D}(i, t_j) &= \|\mathbf{s}_i - \mathbf{h}_{t_j}\| \\ &+ \min [\mathbf{D}(i-1, t_j), \mathbf{D}(i, t_{j-1}), \mathbf{D}(i-1, t_{j-1})]. \end{aligned} \quad (26)$$

The results of DTW are saved in matrix \mathbf{D} , e.g., the distance between the t_j th phase vector from the map and the i th observation vector from the test matrix is placed at the i th row, t_j th column of matrix \mathbf{D} . Considering that all test observations are collected for the same temperature, each column of matrix \mathbf{D} is summed up to depict the distance between the unknown temperature and the temperature candidate corresponding to the column (Step 12). Then, we propose a greedy method to select the estimated temperature. As is shown in Step 14, the temperature with the lowest distance in vector \mathbf{e} is chosen as the estimated temperature t_* .

IV. EXPERIMENTAL STUDY

A. Prototyping and Experiment Configuration

To evaluate the performance of RFThermometer, we implement the system with commodity RFID tags and readers. Any

Algorithm 1 Online Temperature Estimation Algorithm

Input: Phase-temperature map \mathcal{H} and test tensor \mathcal{R}

Output: Temperature estimation t_*

```

1: //Tensor  $\mathcal{R}$  is a sparse tensor with size  $50 \times a \times b$ 
2:  $\mathcal{S} = \text{tensor\_completion}(\mathcal{R})$ ;
3: //Test matrix  $\mathbf{S}$  is the mode-1 unfolding of  $\mathcal{S}$ 
4:  $\mathbf{S} = \mathcal{S}^{(1)}$ ;
5: for  $j = 1 : L$  do
6:   //L: the range of temperatures in the phase-temperature
   map  $\mathcal{H}$ 
7:   for  $i = 1 : a \times b$  do
8:     //a  $\times$  b, the total number of observations in the test
     matrix  $\mathbf{S}$ 
9:      $\mathbf{D}(i, t_j) = \text{DTW}(\mathbf{s}_i, \mathbf{h}_{t_j})$ ;
10:   end for
11: end for
12:  $\mathbf{e} = \sum_i \mathbf{D}(i, t_j)$ ;
13: //Calculate the overall distance between the unknown
   temperature and known temperatures
14:  $t_* = \{t_j \mid e_{t_j} = \min(\mathbf{e})\}$ ;
15: //Choose the temperature with the lowest distance
16: return  $t_*$ ;

```

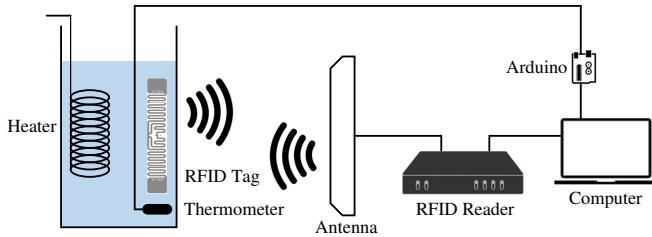


Fig. 8. Experiment configuration of RFThermometer.

RFID reader that is compatible with EPCglobal Class 1 Generation 2 [17] can be used in our proposed RFThermometer system. According to RFID frequency regulations, different numbers of channels are available for different regions in the world. For the US, RFID readers hop among 50 frequencies. In particular, a SMARTRAC R6 DOGBONE tag [33] is attached to a water-filled glass cylindrical container, which has a radius of 4.5cm and a height of 24cm. The tag is interrogated by a Zebra FX9600 reader [21] equipped with a Zebra AN480 antenna [34]. The phase standard deviation of FX9600 is 0.1 degree in radians. A water heater is inserted in the water to control the temperature. A DS18020 temperature sensor is attached to the inner wall of the container and it is connected with an Arduino mega2560 board to provide a real-time temperature report as ground truth. The Robot Operating System (ROS) is leveraged to synchronize the phase data from the RFID reader and the temperature report from the temperature sensor. The implementation of the experimental RFThermometer system is illustrated in Fig. 8.

In the online stage, to avoid uneven temperature distribution caused by the water heater, the water heater is removed when the temperature of water is increased up to 85°C. We monitor the temperature of water and the phase continuously until the temperature decreases to 30°C. In the offline stage, we

collected phase observations from random temperatures to construct the phase-temperature map \mathcal{H} .

B. Accuracy of Temperature Estimation

To evaluate the performance of RFThermometer, the phases are collected from 50 temperatures while the temperature of water is dropping. For each temperature value, 50 reading cycles are conducted, and 30% of the phases in each observation are deleted to imitate the phase loss in practical environments. A training tensor is constructed with phases collected from 70% of the temperature samples, while the remaining phases are leveraged to generate the testing tensor in the online stage. To ensure fairness, the temperature samples are selected randomly. The experiment is conducted 20 times. The results of the experiment show that the average temperature error is 2.6°C and the standard deviation is 0.2 °C.

However, the phases for training and testing are gathered simultaneously, which is not matched with the practical situation of a thermometer. To better verify the performance of RFThermometer in a practical environment, we collect the phases for training and for testing separately, i.e., with a gap of 15 minutes in between the training phase collection and the testing phase collection.

In this experiment, five phase tensors with different sizes are generated to build the phase-temperature map. The phases in each tensor are collected from different numbers of temperatures and different numbers of phases are available for the channels in each tensor. We collect phases from 10, 20, 30, 40, and 50 temperature samples to generate tensors. Moreover, 10, 20, 30, 40, and 50 phase observations are available for each channel of the tensor collected from 10, 20, 30, 40, and 50 temperature samples, respectively.

Fig. 9 presents the CDF of temperature estimation errors obtained from different tensors. The median temperature error is 3°C when the phase-temperature map is constructed by the phases collected from 10 temperatures. We also find the median temperature error remains at 2°C for different maps constructed with phases collected at 20, 30, 40, and 50 temperatures, respectively. It is noteworthy that the tensor collected at 10 temperatures only consists of 10 phase data on each channel, thus we can see that inadequate temperature sampling does not hurt much the performance of RFThermometer. The map could be built with fewer temperature samples and fewer observations in each channel, which means that the cost of building a map can be significantly reduced. Moreover, the temperature errors are under 8°C for 88% of testing data for all the maps. These results validate the robustness of RFThermometer. For the map constructed with phases obtained from 50 temperatures, about 96% of estimation errors are less than or equal to 3°C.

To better evaluate the accuracy of our RFThermometer system, a Ryobi IR002 infrared thermometer is compared with our RFThermometer. Because the IR002 thermometer cannot provide a continuous temperature report, 10 temperature inspection points are chosen to evaluate the accuracy of two systems. For RFThermometer, phase-temperature maps are constructed with phases collected from 8 temperature

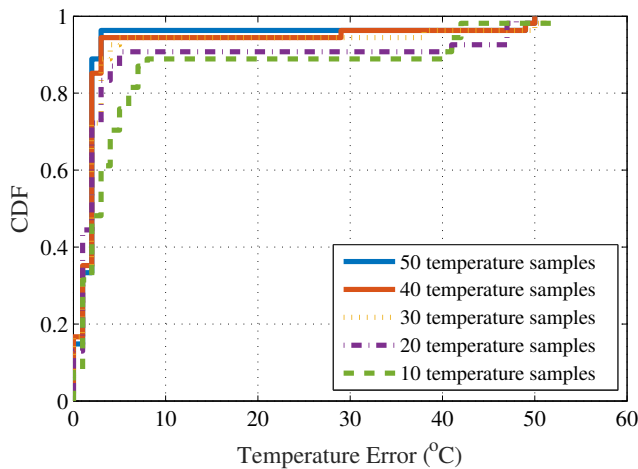


Fig. 9. CDF of temperature estimation errors for RFThermometer using phases sampled from different numbers of temperatures.

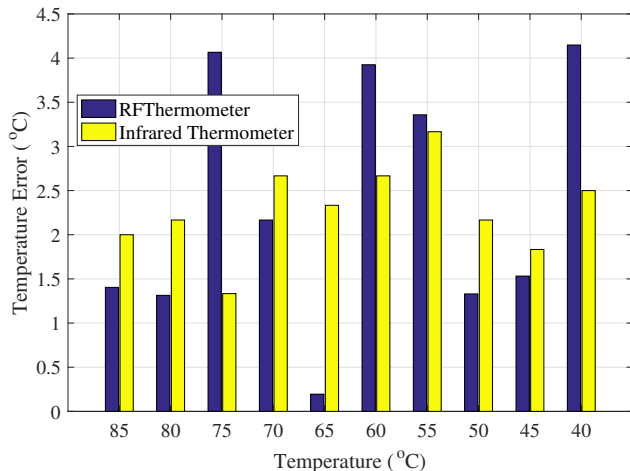


Fig. 10. Temperature Errors of RFThermometer and Infrared Thermometer in 10 inspection points.

samples. 10 observations are available in each phase tensor. The comparison result is shown in Fig. 10. We find the RFThermometer is more accurate than Ryobi IR002 infrared thermometer at inspection points of 85°C, 80°C, 70°C, 65°C, 50°C and 45°C. However, RFThermometer does not show an outstanding performance at the rest of inspection points. The average temperature error for Ryobi IR002 infrared thermometer is 2.2833°C, while the average temperature error is 2.34°C for RFThermometer. The result exhibits that the average precision of RFThermometer is comparable to the commercial infrared thermometer. Note that in this experiment, the manually chosen inspection points exclude extreme points (i.e. the temperature higher than 85°C and lower than 40°C), which will be included in following experiments. Therefore, the result of this experiment is better than those of the following experiments.

C. Impact of Various Design Parameters

1) *Impact of Tensor Completion:* The effect of tensor completion on the mean temperature error is shown in Fig. 11.

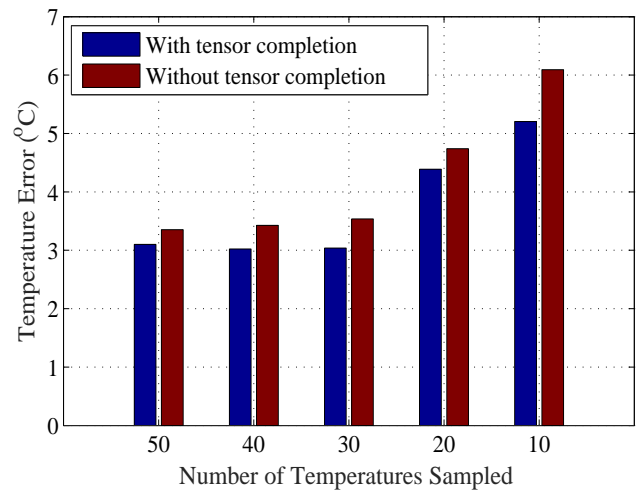


Fig. 11. Mean temperature estimation errors with and without the tensor completion method.

Similarly, 5 tensors are utilized to evaluate the effect. The red bars represent the mean temperature errors obtained by the maps that are constructed without tensor completion, while the blue bars are calculated by the maps that are generated with tensor completion. Even though the temperature error goes high when fewer temperatures are sampled for map construction, the largest error is only about 5.2°C, which occurs when the map is constructed with a phase tensor that is processed by the tensor completion and is collected from 10 temperatures. Similarly, only 10 observations are available in each channel in this phase tensor. Such error is acceptable in most cases that does not require a precise temperature estimation. The lowest error is about 3.022°C when the phases obtained from 40 temperatures are used to build the map. However, the high precision relies on the laborious data collection in the offline stage. Thus, the estimation precision and the labor cost are a trade-off here. Furthermore, it is obvious that all the red bars are higher than the corresponding blue bars, indicating that the phases restored by tensor completion help Gaussian Process to build a more precise phase-temperature map.

2) *Impact of the Number of Observations of Training Tensor:* To investigate the impact of the number of observations on temperature estimation, we tailored the phase tensor before tensor completion. All phase tensors include phases collected from 39°C, 46°C, 53°C, 60°C, 67°C, 74°C, 81°C, and 88°C. To imitate the phase losses in a complex environment, 70 phases in each channel are randomly deleted. And 20 experiments are conducted with each number of observations.

As shown in Fig. 12, the number of observations does not significantly affect the mean temperature estimation error. All temperature estimation errors are around 5.5°C. The lowest error, 4.9°C, occurs when the tensor is comprised of phases collected from 8 reading cycles. The error is 5.5°C when the tensor includes the phases collected from 3 observations. The temperature error is 5.8°C when the tensor contains 50 observations. Thus, the temperature error is not greatly affected by the increasing number of observations. We also notice that the standard deviation of temperature estimation

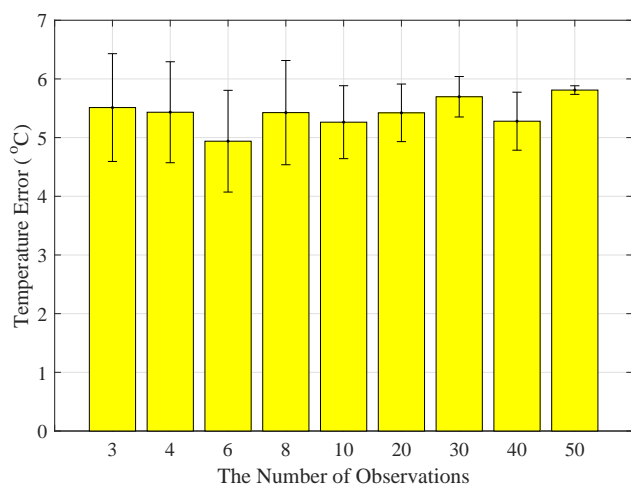


Fig. 12. Mean temperature estimation errors with different numbers of observations.

errors decreases slightly when more observations are used. With 50 observations, the lowest standard deviation, 0.07°C , is achieved. The highest standard deviation, 0.91°C , occurs when phases collected with 3 observations. Thus, it is safe to say that the number of observations does not significantly influence the estimation precision of RFThermometer. According to [21], the FX9600 reader is able to complete a reading cycle within a period of 5 seconds. Therefore, an acceptable temperature estimation could be obtained by our RFThermometer with a data collection stage that takes 15 seconds at most in each temperature. In other words, the time consumption for data collecting is reduced remarkably.

3) *Impact of the Percentage of Deleted Phases in the Training Tensor:* We next design a specific experiment by setting different percentages of deleted phases in each channel to evaluate their impact on temperature error. All the phase tensors in this experiment are generated with the phases collected from 8 temperatures and each tensor includes only three observations. Furthermore, 10%, 30%, 50%, 70%, 90% phases in each observation are deleted to investigate the impact of missing phases. For each percentage of deleted phases, the experiment is repeated 20 times to ensure credible results.

Fig. 13 depicts the average temperature errors for increased percentage of deleted phases. It can be seen that the temperature error does not grow dramatically with increased percentage, until 90% phases are deleted on each channel. When the percentage of deleted phases is below 90%, the average temperature error is 5.3°C . The minimum temperature error, 5.1°C , happens when 10% of the phases are deleted on each channel. When the percentage of deleted phases is 90%, the temperature error escalates to 9.0°C . Meanwhile, the standard deviation of the temperature error also goes up with the deletion percentage. Similar to temperature error, the standard deviation increases from 0.4°C to 0.9°C when the deletion percentage is below 90%. The maximum standard deviation, 2.5°C , occurs when 90% of the phases are deleted.

According to the results of this experiment, RFThermometer exhibits great robustness when a large part of phases is unavailable, which is meaningful for practical environments.

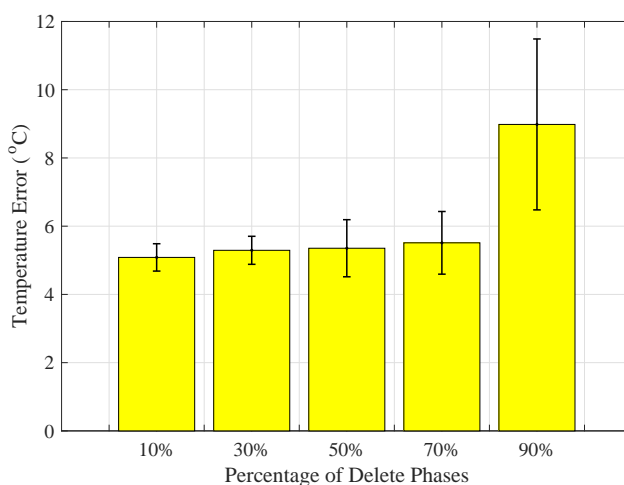


Fig. 13. Mean temperature estimation errors with different percentages of deleted phases.

In such environments, a bunch of tags and readers are usually deployed, which result that and it is challenging to gather all the phases for a tag in one observation. The temperature error remains low when only 30% of phase are available in each observation. That is, the precision of temperature estimation can be guaranteed even with inadequate phase data.

4) *Impact of Map Resolution:* To study the impact of map resolution on temperature error, 5 sets of maps with different temperature intervals (i.e., resolution) are generated with RFThermometer. To ensure fairness, all the maps are constructed with the same phase tensor. Similar to the previous experiments, the phase tensor contains the phases collected from 8 temperature samples. Furthermore, the tensor includes 10 observations for each temperature, and 70% of the phases in each observation are deleted to imitate the phase losses in a practical environment. Each set of maps is comprised with 10 maps with an identical resolution. We choose 5 different temperature intervals for the maps to investigate the impact of map resolution on temperature error.

As shown in Fig. 14, the lowest mean temperature error, which is 5.1°C , is obtained with the maps that have a temperature interval of 1°C , and the corresponding standard deviation is 0.63°C . With increased temperature interval, the average temperature error goes up significantly. For the maps with a temperature interval of 2°C , the error increases to 8.9°C , which is about twice of the lowest error. The largest error occurs when the temperature interval is 5°C . When map resolutions are below 5°C , the standard deviations remains around 0.5°C ; but it increases to 1.4°C when the temperature interval is 5°C . Clearly a high-resolution map ensures more precise temperature estimation.

However, the price for temperature estimation using a high-resolution map, is the estimation latency. The average time consumption in temperature estimation is presented in Fig. 15. Fig. 14 shows that the lowest temperature estimation error is obtained when the temperature interval is 1°C , while Fig. 15 shows that the corresponding time consumption of the online stage is 9.42 s. The estimation latency is inversely proportional

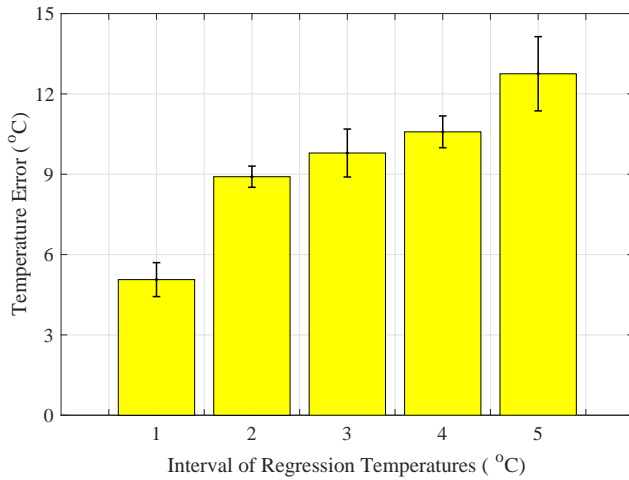


Fig. 14. Mean temperature estimation errors with different temperature intervals in the phase-temperature map.

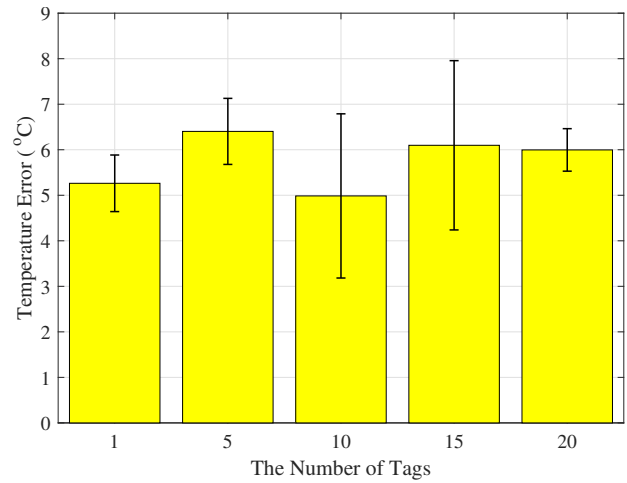


Fig. 16. The average temperature error with different number of tags in the interrogating area.

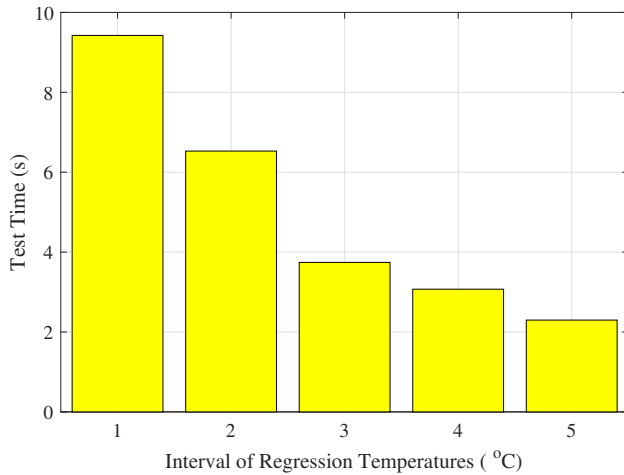


Fig. 15. The average test time with different temperature intervals in the phase-temperature map.

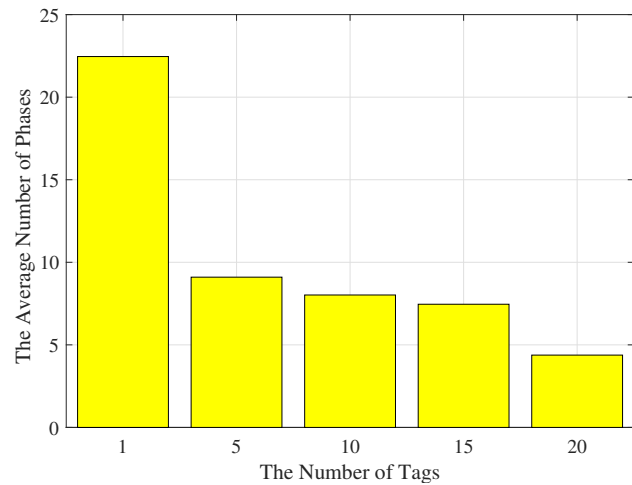


Fig. 17. The average number of phase readings with different number of tags in the interrogating area.

to the temperature interval of phase-temperature map.

5) *Impact of the Number of Tags*: To verify the robustness of our RFThermometer system, we further test the system in an experiment where more than one tags are deployed. Similar to the previous experiments, the phases are collected from 8 temperature samples, and 20 observations are included in each phase tensor. But we employ 1, 5, 10, 15, and 20 tags in the interrogating area to mimic a multiple-tag environment. To avoid the randomness in experiments, each experiment is repeated for 10 times with each group of tags. The mean errors are the bars and the standard deviation are plotted as error bars. As shown in Fig. 16, the mean temperature error is not affected by the number of tags significantly. Even though the mean errors increase when 5, 15, and 20 tags are deployed in the interrogating area, the error reaches the lowest value when 10 tags are present in the experiment. For the standard deviation of temperature errors, 1.803°C and 1.859°C occur when 10 and 15 tags are in the interrogating area, respectively. However, the deviation is 0.4667°C when 20 tags are interrogated by the reader, which is even smaller

than the deviation of temperature error of the one tag case.

We also investigate the availability of phases in this multiple-tag environment. In the experiment, the tags are interrogated within a period of 10 seconds. Fig. 17 depicts the average number of available phase readings in each channel. It shows that plenty of readings are available when there is only one tag in the interrogation area. When the number of tags in the interrogation area is increased, the number of phase readings in each channel decreases significantly. When 20 tags are within the interrogation area, the average number of available phase samples drops to 4.38. Considering that each training tensor contains 20 observations, most of phases are lost when 20 tags are within the interrogation area. However, the decline of available phase readings does not affect the temperature estimation of the RFThermometer system. Fig. 16 demonstrates that the RFThermometer system is able to provide a reliable temperature estimation in a multiple-tag environment.

V. CONCLUSIONS

In this paper, we presented RFThermometer for remote temperature measurement using commodity RFID tags. To mitigate the effect of missing phases, a tensor completion based method was employed to restore the missing phases. The RFThermometer system also employed Gaussian Process to construct a phase-temperature map with the phases restored by tensor completion in the offline stage, and a DTW based greedy method to estimate the unknown temperature in the online stage. We evaluated the performances of RFThermometer with commodity RFID tags and reader. The experimental results showed that RFThermometer was capable of building reliable phase-temperature maps with only a small amount of phase measurements, and that tensor completion effectively improved the temperature estimation precision.

REFERENCES

- [1] J. Zhang, Y. Lyu, J. Patton, S. C. Periaswamy, and T. Roppel, "BFVP: A probabilistic UHF RFID tag localization algorithm using Bayesian filter and a variable power RFID model," *IEEE Transactions on Industrial Electronics*, vol. 65, no. 10, pp. 8250–8259, Oct. 2018.
- [2] S. Pradhan, E. Chai, K. Sundaresan, L. Qiu, M. A. Khojastepour, and S. Rangarajan, "RIO: A pervasive RFID-based touch gesture interface," in *Proc. ACM MobiCom'17*, Snowbird, UT, Oct. 2017, pp. 261–274.
- [3] X. Wang, C. Yang, and S. Mao, "SparseTag: High-precision backscatter indoor localization using sparse RFID tags array," pp. 1–9, preprint, currently under review.
- [4] J. Zhang, Z. Yu, X. Wang, Y. Lyu, S. Mao, S. C. Periaswamy, J. Patton, and X. Wang, "RFHUI: An intuitive and easy-to-operate human-UAV interaction system for controlling a UAV in a 3D space," in *Proc. EAI MobiQuitous 2018*, New York City, NY, Nov. 2018, pp. 1–8.
- [5] J. Zhang, Z. Yu, X. Wang, Y. Lyu, S. Mao, S. Periaswamy, J. Patton, and X. Wang, "RFHUI: An RFID based human-unmanned aerial vehicle interaction system in an indoor environment," *Elsevier Digital Communications and Networks Journal*, 2019.
- [6] J. Wang, J. Xiong, X. Chen, H. Jiang, R. K. Balan, and D. Fang, "TagScan: Simultaneous target imaging and material identification with commodity RFID devices," in *Proc. ACM MobiCom'17*, Snowbird, Utah, Oct. 2017, pp. 288–300.
- [7] C. Yang, X. Wang, and S. Mao, "AutoTag: Recurrent vibrational autoencoder for unsupervised apnea detection with RFID tags," in *Proc. IEEE GLOBECOM 2018*, Abu Dhabi, United Arab Emirates, Dec. 2018, pp. 1–7.
- [8] K. Opasjumruskit *et al.*, "Self-powered wireless temperature sensors exploit RFID technology," *IEEE Pervasive Comput.*, no. 1, pp. 54–61, Feb. 2006.
- [9] A. Vaz *et al.*, "Full passive UHF tag with a temperature sensor suitable for human body temperature monitoring," *IEEE Trans. Circuits Syst. II, Exp. Briefs*, vol. 57, no. 2, pp. 95–99, Feb. 2010.
- [10] A. A. Babar, S. Manzari, L. Sydanheimo, A. Z. Elsherbeni, and L. Ukkonen, "Passive UHF RFID tag for heat sensing applications," *IEEE Transactions on Antennas and Propagation*, vol. 60, no. 9, pp. 4056–4064, Sept. 2012.
- [11] K. Zannas, H. El Matbouly, Y. Duroc, and S. Tedjini, "On the cooperative exploitation of antenna sensitivity and auto-tuning capability of UHF RFID chip. Application to temperature sensing," in *2018 IEEE/MTT-S International Microwave Symposium*, Philadelphia, PA, June 2018, pp. 374–377.
- [12] —, "Self-tuning RFID tag: A new approach for temperature sensing," *IEEE Transactions on Microwave Theory and Techniques*, vol. 66, no. 12, pp. 5885–5893, Dec. 2018.
- [13] X. Wang, L. Gao, and S. Mao, "CSI phase fingerprinting for indoor localization with a deep learning approach," *IEEE Internet of Things Journal*, vol. 3, no. 6, pp. 1113–1123, Dec. 2016.
- [14] Y. Zheng, Y. He, M. Jin, X. Zheng, and Y. Liu, "RED: RFID-based eccentricity detection for high-speed rotating machinery," in *Proc. IEEE INFOCOM'18*, Honolulu, HI, Apr. 2018, pp. 1565–1573.
- [15] J. Wang, D. Vasisht, and D. Katabi, "RF-IDraw: Virtual touch screen in the air using RF signals," in *ACM SIGCOMM'14*, Chicago, IL, Aug. 2014, pp. 235–246.

- [16] X. Wang, J. Zhang, Z. Yu, E. Mao, S. C. Periaswamy, and J. Patton, "RFThermometer: A temperature estimation system with commercial UHF RFID tags," in *Proc. IEEE ICC 2019*, Shanghai, China, May 2019, pp. 1–6.
- [17] *Radio-Frequency Identity Protocols Class-1 Generation-2 UHF RFID Protocol for Communications at 860 MHz - 960MHz*, Accessed on May. 20, 2019. [Online]. Available: https://www.gs1.org/sites/default/files/docs/epc/uhf1g2_1_2_0-standard-20080511.pdf
- [18] J. A. Bengua, H. N. Phien, H. D. Tuan, and M. N. Do, "Efficient tensor completion for color image and video recovery: Low-rank tensor train," *IEEE Trans. Image Process.*, vol. 26, no. 5, pp. 2466–2479, May 2017.
- [19] J. Liu, P. Musialski, P. Wonka, and J. Ye, "Tensor completion for estimating missing values in visual data," *IEEE Trans. Pattern Anal. Mach. Intell.*, vol. 35, no. 1, pp. 208–220, Jan. 2013.
- [20] N. Kreimer and M. D. Sacchi, "A tensor higher-order singular value decomposition for prestack seismic data noise reduction and interpolation," *Geophysics*, vol. 77, no. 3, pp. V113–V122, May 2012.
- [21] *Zebra FX9600 Reference Guide*, Accessed on Oct. 14, 2018. [Online]. Available: https://www.zebra.com/content/dam/zebra_new_ia/en-us/manuals/rfid/fx9600-qrg-en.pdf
- [22] C.-H. Loo *et al.*, "Chip impedance matching for UHF RFID tag antenna design," *Prog. Electromagn. Res.*, vol. 81, pp. 359–370, 2008.
- [23] X. Wang, C. Yang, and S. Mao, "Tensorbeat: Tensor decomposition for monitoring multi-person breathing beats with commodity WiFi," *ACM Trans. Intell. Syst. Technol.*, vol. 9, no. 1, pp. 8:1–8:27, Sept. 2017.
- [24] T. G. Kolda and B. W. Bader, "Tensor decompositions and applications," *SIAM Review*, vol. 51, no. 3, pp. 455–500, Aug. 2009.
- [25] V. De Silva and L.-H. Lim, "Tensor rank and the ill-posedness of the best low-rank approximation problem," *SIAM J. Matrix Analysis Appl.*, vol. 30, no. 3, pp. 1084–1127, Sept. 2008.
- [26] Z. Zhang, G. Ely, S. Aeron, N. Hao, and M. Kilmer, "Novel methods for multilinear data completion and de-noising based on tensor-SVD," in *Proc. IEEE CVPR'14*, Columbus, OH, June 2014, pp. 3842–3849.
- [27] E. J. Candès and B. Recht, "Exact matrix completion via convex optimization," *Found. Computat. Math.*, vol. 9, no. 6, pp. 717–772, Apr. 2009.
- [28] M. E. Kilmer, K. Braman, N. Hao, and R. C. Hoover, "Third-order tensors as operators on matrices: A theoretical and computational framework with applications in imaging," *SIAM J. Matrix Analysis Appl.*, vol. 34, no. 1, pp. 148–172, Feb. 2013.
- [29] O. Semerci, N. Hao, M. E. Kilmer, and E. L. Miller, "Tensor-based formulation and nuclear norm regularization for multienergy computed tomography," *IEEE Trans. Image Process.*, vol. 23, no. 4, pp. 1678–1693, Apr. 2014.
- [30] W. Hu, D. Tao, W. Zhang, Y. Xie, and Y. Yang, "The twist tensor nuclear norm for video completion," *IEEE Trans. Neural Netw. Learning Syst.*, vol. 28, no. 12, pp. 2961–2973, Dec. 2017.
- [31] S. Boyd *et al.*, "Distributed optimization and statistical learning via the alternating direction method of multipliers," *Foundations and Trends® in Machine Learning*, vol. 3, no. 1, pp. 1–122, Jan. 2011.
- [32] C. E. Rasmussen, "Gaussian processes in machine learning," in *Advanced Lectures on Machine Learning*, O. Bousquet, U. von Luxburg, and G. Ratsch, Eds. Berlin, Heidelberg: Springer, 2004, pp. 63–71.
- [33] *SMARTRAC R6 DOGBONE Datasheet*, Accessed on Oct. 14, 2018. [Online]. Available: http://rfid.atlasrfidstore.com/hubfs/Tech_Spec_Sheets/Smarttrac/ATLAS_Dogbone_R6.pdf
- [34] *Zebra RFID Antenna Family Datasheet*, Accessed on Oct. 15, 2018. [Online]. Available: <https://cdn.barcodeinc.com/themes/barcodeinc/pdf/Motorola/an-series.pdf>



Xiangyu Wang received the B.S. degree in electrical engineering from Taiyuan Institute of Technology, Taiyuan, China in 2014, and an MS degree in Electrical and Computer Engineering (ECE) from Auburn University, Auburn, AL in 2017. He has been pursuing a PhD in ECE at Auburn University since Spring 2018. His research interests focus on machine learning, indoor localization, and IoT. He is a co-recipient of the Best Student Paper Award of IEEE PIMRC 2017.



Jian Zhang received the B.Sc. and M.Sc. degrees in Applied Physics from Sichuan University, Chengdu, China, in 2001 and 2008, respectively. He received the Ph.D. in the Electrical and Computer Engineering from the Auburn University, Auburn, AL USA in 2016. Currently, he is a Postdoctoral Research Fellow in the RFID Lab at Auburn University. His main research interests include RFID technologies and applications, Internet of Things, indoor localization, UAV and collaborative robotics. His work

has focused on improving the efficiency of supply chain management for the industry and the business.



Senthilkumar CG Periaswamy received the Ph.D. in Computer Science from University of Arkansas Fayetteville in 2010. He is currently the Director of Technology for the RFID lab at Auburn University, a unique collaboration platform that involves end users, suppliers, technology providers, standards organizations, industry groups, and academic institutions on a global scale. He has researched, advised, and executed projects that is enabling efficient adoption of RFID and sensor fusion in retailing, aerospace, manufacturing, and transportation. His

work has focused on the common goal of making the adaptation of RFID and related sensor technologies more secure, efficient, reliable and useful.



Zhitao Yu received a B.S. degree in electrical engineering from Nanjing University of Posts and Telecommunication, Nanjing, China in 2016, and an MS degree in Electrical and Computer Engineering from Auburn University, Auburn, AL in 2018. He has been pursuing a PhD in ECE at Auburn University since Spring 2019. His research interests include indoor localization, deep learning and UAV indoor navigation. Currently he is a research assistant in the RFID lab, Auburn University.



Shiwen Mao [S'99-M'04-SM'09-F'19] received his Ph.D. in electrical and computer engineering from Polytechnic University, Brooklyn, NY (now The New York University Tandon School of Engineering). He was the McWane Associate Professor in the Department of Electrical and Computer Engineering at Auburn University, Auburn, AL from 2012 to 2015. Currently, he is the Samuel Ginn Distinguished Professor and Director of the Wireless Engineering Research and Education Center at Auburn University.

His research interests include wireless networks, multimedia communications, and smart grid. He is a Distinguished Speaker of the IEEE Vehicular Technology Society. He is an Area Chair of IEEE Open Journal of the Communications Society and IEEE Internet of Things Journal, and an Associate Editor of IEEE Transactions on Network Science and Engineering, IEEE Transactions on Mobile Computing, IEEE Transactions on Multimedia, IEEE Internet of Things Journal, IEEE Multimedia, IEEE Networking Letters, and ACM GetMobile, among others.

He received the IEEE ComSoc TC-CSR Distinguished Technical Achievement Award in 2019, the IEEE ComSoc MMTC Distinguished Service Award in 2019, Auburn University Creative Research & Scholarship Award in 2018, the 2017 IEEE ComSoc ITC Outstanding Service Award, the 2015 IEEE ComSoc TC-CSR Distinguished Service Award, and the 2013 IEEE ComSoc MMTC Outstanding Leadership Award, and NSF CAREER Award in 2010. He is a co-recipient of the IEEE ComSoc MMTC Best Journal Paper Award in 2019, the IEEE ComSoc MMTC Best Conference Paper Award in 2018, the Best Demo Award from IEEE SECON 2017, the Best Paper Awards from IEEE GLOBECOM 2016 & 2015, IEEE WCNC 2015, and IEEE ICC 2013, and the 2004 IEEE Communications Society Leonard G. Abraham Prize in the Field of Communications Systems. He is a Fellow of the IEEE.



Justin Patton is the Director of the Auburn University RFID Lab, a research institute focusing on the business case and technical implementation of emerging technologies in retail, supply chain, aerospace, and manufacturing. The RFID Lab is a unique private/academic partnership between users, technology vendors, standards organizations, and faculty. Justin has participated in business case research for advanced technology with Walmart, Target, Amazon, FedEx, Dillards, Macys, Delta Air Lines, and Boeing among others, and is currently

researching upstream supply chain benefits of RFID in both retail and manufacturing. He is one of the primary developers of the ARC program, the first and most widely utilized international performance validation system for RFID, and is currently working to help standardize the process of testing and certifying RFID performance in all aspects of the supply chain.